Frictional and transport properties of the Chelungpu fault from shallow borehole data and their correlation with seismic behavior during the 1999 Chi-Chi earthquake

Wataru Tanikawa[1]*

Toshihiko Shimamoto[2]

1 Kochi Institute for Core Sample Research, Japan Agency for Marine-Earth Science and Technology, Nankoku, Japan

2 Department of Earth and Planetary Systems Science, Graduate School of Science, Hiroshima University, Higashi-Hiroshima, Japan

*Corresponding author

Address: Kochi Institute for Core Sample Research, Japan Agency for Marine-Earth Science and Technology, Nankoku 783-8502, Japan

Tel: +81-88-878-2203; fax: +81-88-878-2192

E-mail: tanikawa@jamstec.go.jp

Abstract

We carried out low- and high-velocity friction tests on fault rock samples from shallow boreholes on the Taiwan Chelungpu fault and measured their fluid transport properties under high pressure with the objective of explaining the different seismic behavior in northern and southern sections of the fault during the 1999 Chi-chi earthquake. Our results of low-velocity friction tests demonstrate that fault gouge from the southern section of the fault exhibits velocity-weakening frictional behavior, whereas gouge from the northern section exhibits velocity-strengthening friction. Friction in the northern gouge decreased strongly with increasing wetness, whereas friction in southern gouge samples was not affected by wetness. A rapid reduction of friction was observed immediately after the onset of slip in high-velocity friction tests. The results of high-velocity friction tests were similar for all fault gouge samples tested, though permeability in the northern fault zone was lower than that in the south. Numerical modeling indicated that thermal pressurization in the northern fault zone promoted stress reduction and fault instability during slip, whereas it did not in the south. This contrasting seismic behavior between north and south is caused mainly by differences in fluid transport properties of the slip zones. More efficient thermal pressurization in the north explains the large slip displacement there. The results of our low-velocity friction

tests are consistent with nucleation of the Chi-Chi earthquake in the south and propagation of the rupture from south to north.

1. Introduction

The rupture along the 100-km-long Chelungpu fault in the western Taiwan basin during the 1999 Chi-Chi earthquake (M_w 7.6) was unusual in that there was considerable difference in slip behavior between the southern and northern parts of the fault. Strong motion records and co-seismic GPS measurements revealed a low acceleration and large slip displacement along the northern part of the fault on the surface (up to 9.8 m horizontally, 5.6 m vertically), and a high acceleration and small slip displacement (3.5 m horizontally, 4 m vertically) along the southern part [*Lee et al.*, 2002; *Ma et al.*, 2003]. The largest accelerations, some greater than 1*g*, were in the southern part of the fault, where the rupture initiated, and they decreased to about 0.5*g* toward the northern part of the fault [*Shin and Teng*, 2001]. The largest slip velocities of up to 3.0 m/s were observed in the northern section of the Chelungpu fault. Inversion analysis using teleseismic data indicated that there was a large reduction in dynamic stress associated with the large amount of slip on the northern section of the fault [*Ma et al.*, 2000]. Two shallow boreholes were drilled into the fault at a northern site

(Fengyuan) and a southern site (Nantou) to investigate the factors controlling the north–south contrast of seismic slip behavior (Figure 1, 2) [*Tanaka et al.,* 2002; *Tanaka et al.*, 2006a]. At the northern site (total depth 455 m), three major fault zones that are candidate faults for slip during the 1999 Chi-Chi earthquake are developed within the Kueichulin Formation and Chinshui Shale at 224.55–224.80 m, 328.55–330.00 m, and 416.00–417.90 m. (FZ-A, FZ-B, FZ-C in Figure 2). One of the candidate horizons (330 m depth) is at the base of a thick fracture zone (285–330 m depth) in the Kueichulin Formation, where the fault zone consists of thick fault breccias and a very thin (7 mm thickness), clay-rich gouge layer. Within the fault gouge layer, preferred alignments of phyllosilicate minerals associated with grain-size fining were observed, though there was little microstructural evidence of frictional melting [*Tanaka et al.*, 2006a]. In contrast, a possible slip horizon observed in the southern borehole (total depth 211 m) lies at 175–177 m depth beneath a thick foliated fault breccia zone (154–177 m) between the Chinshui Shale and the Toukoshan Formation (Figure 1d, FZ-D in Figure 2). The possible center of the fault zone consists of ultracataclasite with some pseudotachylyte [*Otsuki and Monzawa,* 2001], and the ultracataclasite indicates a thin (up to 0.5 mm) and localized shear zone. The other possible slip zone in the southern borehole is within a brown and gray clay layer lies at 179.9 m to 183.2 m (Hashimoto et al., 2007), though the shear localization was not recognized. A part of the fault zone (175.3–175.9 m, 176.8–177.3 m) was not recovered in the southern borehole, therefore the other slip candidates might be within the missing portions. Structural analysis [*Yue et al.*, 2005] suggests that this structural and lithologic contrast between northern and southern slip zones is preserved to at least 3 km depth. Therefore, the differences in the texture and other physical characteristics of the faulted rocks of the northern and southern boreholes may have influenced frictional and transport properties (permeability, porosity, and specific storage) and would thus account for the differences in slip behavior.

Temperature measurements in the shallow boreholes [*Tanaka et al.,* 2002, 2006a] were slightly anomalous in the possible slip zones (Figure 2). *Tanaka et al.* [2006a] proposed that they could be explained by very low friction (coefficient of friction from 0.05 to 0.12). *Kano et al.* [2006] conducted similar temperature measurements at 1200 m depth in a deeper northern borehole that was drilled as part of the Taiwan Chelungpu Fault Drilling Project (TCDP) and also concluded that very low friction slip might have occurred during the 1999 Chi-Chi earthquake. However, neither of these studies presented friction data from laboratory tests on recovered samples to verify their assertions of low-friction slip.

In laboratory tests, *Di Toro et al.* [2004] showed that friction at high velocities, approaching seismic velocity, is very different from conventional low-velocity friction that obeys the rate and state friction low [*Dietrich*, 1978, 1979]. In some cases, the difference is attributed to rapid heating to the melting point within fault zones during high-velocity slip [*Tsutsumi and Shimamoto*, 1997; *Hirose and Shimamoto*, 2005]. In addition, such a temperature rise can cause chemical reactions within the slip zone that may be associated with fault weakening [*Han et al.*, 2007]. *Hirono et al.* [2006, 2008] reported evidence of chemical reactions as a result of frictional heating in the Chelungpu fault, but did not identify melt structures.

Transport properties within a fault zone also have an important influence on dynamic slip motion. Increased pore pressure induced by frictional heating ("thermal pressurization" hereafter) can cause fault weakening [*Sibson*, 1973]. Transport properties can vary by several orders of magnitude for different rock types [*Neuzil*, 1994]; therefore, the thermal pressurization mechanism is probably controlled primarily by transport properties rather than thermal conditions. Recent studies [*Wibberley*, 2002; *Noda and Shimamoto*, 2005; *Wibberley and Shimamoto*, 2005] have reported that fault rocks can potentially cause thermal pressurization when hydraulic diffusivity in the fault zone is low and the width of the slip zone is very thin.

In this study, we measured the frictional properties of fault gouge samples from the shallow northern and southern boreholes, and from outcropping fault gouge from the Shuangtung fault, at low and high rates of strain. Transport properties of the fault rocks and surrounding host rocks from the northern and southern boreholes were measured under high pressure. We used measured frictional and transport properties as inputs in a numerical model of thermal pore fluid pressurization.. Finally, we discuss the contrasting seismic slip behavior during the 1999 Chi-Chi earthquake on the basis of our laboratory data and numerical modeling results.

2. Experimental Methods

2.1. Samples

For friction tests, we used dark gray ultracataclasite from 176.8 m depth in the southern borehole, and samples from a 10-cm-thick, clay-rich fault gouge from 286 m depth in the northern borehole. We also used fault gouge from 330 m depth for high-velocity friction test. The fault zone at 286 m depth in the northern borehole may not be within the candidate slip zone for the 1999 Chi-Chi earthquake, though the fault zone is within the thick fracture zone (285–330 m depth) where the positive thermal anomaly was observed. However, we consider it to be analogous to the slip zone because of the relatively large proportion of clay minerals, which may have developed as a result of shear deformation, and because the host rocks for these fault gouge samples were within the Kueichulin Formation, as is the case for the candidate slip zone (FZ-B and FZ-C).

Crushed gouge samples of grain size <0.12 mm were used for friction tests. The fault gouge from 286 m depth in the northern borehole contains much smectite, as well as illite and kaolinite, as determined by x-ray diffraction (XRD) (Figure 3a). Black cataclasite from the southern fault consists mainly of quartz with a lower clay mineral content than the northern borehole.

Transport properties of the host and fault rocks in the northern and southern shallow boreholes were measured. In the north, host rock is sandstone and siltstone composed mostly of quartz, feldspar, calcite, and clay minerals (illite, smectite, and muscovite). In the south, the footwall of the Chelungpu fault is Toukoshan Formation, and is composed mainly of conglomerate with a clayey to silty matrix. Even though we were unable to recover complete sections through the fault zones in both shallow boreholes, we consider that the transport properties we measured covered a representative sample of host and fault rocks.

2.2. Low-velocity Friction Tests

We performed shearing experiments by placing two layers of gouge between gabbro blocks in a double-direct shear apparatus (Figure 3c) to measure conventional low frictional properties [*Kawamoto and Shimamoto*, 1998]. In this experiment, we used 1.5 to 2 g of crushed gouge, corresponding to a thickness of about 1 mm, for each layer. Three stainless steel blocks completed the apparatus; the center block was placed on top of the central gabbro block and the other blocks were placed adjacent to the gabbro blocks on each side. Typically, experiments were performed until the total displacement reached the limit of the apparatus (20 mm). Experiments were performed at room temperature under “dry” (room humidity; typically 40%–60% relative humidity [RH]) or “wet” (100% RH) conditions. The gouge layers were saturated with distilled water after the apparatus was set up to achieve 100% RH in the gouge layer.

Before the vertical piston (the stainless steel block on top) was moved to apply shear force, a normal stress of about 1.5 times the target normal stress was applied to the sample. The shear load was then cycled two or three times at a constant velocity of 1 to 5 μm/s (Figure 3b). This load cycle helps to localize shear and results in steady-state friction being reached with less net displacement than if the test is conducted without shear load cycles [*Frye and Marone*, 2002]. After steady-state friction was achieved, velocity-stepping experiments were performed. Then, a slide-hold-slide test was performed until the limit of displacement (20 mm) was reached. Typically, we performed two series of velocity-stepping tests, with the velocity changing rapidly by 1 order of magnitude at each velocity step change (i.e., one series of velocity step changes was 0.15 →1.5 →15 →150→15 →1.5 →0.15 μm/s). To achieve a new steady-state condition in response to each velocity step change, 0.5 to 1 mm of slip was required.

The friction coefficient is determined from the ratio of shear stress to normal stress. The steady-state velocity dependence, or friction rate dependence, ($a - b$), is a key parameter of fault dynamics. The parameter ($a - b$) is evaluated from the imposed velocity step test results by the following equation:

$$\mu_{ss}(V) - \mu_{ss}(V^*) = (a-b)\ln\left(\frac{V}{V^*}\right), \quad (1)$$

where $\mu_{ss}(V^*)$ is the steady-state friction coefficient at a prescribed speed V^*, and $\mu_{ss}(V)$ is the steady-state friction coefficient at a velocity V imposed by a step change in sliding speed. If the material is velocity-strengthening, then $(a - b) > 0$, and the system is intrinsically stable. If the material is velocity-weakening, then $(a - b) < 0$, and the fault may exhibit unstable behavior. In the stable regime, rupture nucleation and propagation are inhibited. An earthquake can propagate in both cases, but rupture nucleation occurs only in an unstable field, which requires velocity-weakening friction

(Rice and Ruina, 1983).

2.3. High-velocity Friction Tests

We performed high-velocity friction tests on gouge samples (from the same sources as those used for the low-velocity tests) using the high-speed rotary-shear testing apparatus of *Shimamoto and Tsutsumi* [1994] and the methodology of *Mizoguchi et al.* [2007]. A 1-g sample of gouge was placed between a pair of calcite-cemented quartz-rich sandstone cylinders (0.2 mm average grain size, 10% porosity, 10^{-17} m^2 permeability) of about 25 mm diameter, of which the rough end surfaces had been smoothed by grinding with #80 silicon carbide powder (Fig. 3d). A gouge layer about 1 mm thick was sheared by rotating one of the cylinders. A Teflon sleeve was used to cover the simulated fault plane so that the gouge was confined between the sandstone surfaces during shearing. The samples were dried in an oven at 80 °C before the experiment to eliminate the pore water within samples, though they were exposed to a humid environment during the experiment. For all tests, we used a constant rotational speed of 1200 rpm and constant normal stress from 0.6 to 0.9 MPa. Slip rate varies within the apparatus as a function of distance from the center of the axis of rotation; slip displacement and slip rate are zero at the center of the sample and largest at the edge of the sample. For our test conditions, slip velocity was 1.96 m/s at the edge of the sample. When we define an equivalent slip velocity, Veq, such that a total friction work on a fault area S is described as $\tau \cdot V_{eq} \cdot S$ [*Shimamoto and Tsutsumi*, 1994] where we assume that shear stress τ is constant over the fault surface, V_{eq} was 1.06 m/s for our tests.

2.4. Transport Property Measurements

We measured the fluid transport properties of permeability, porosity, and specific storage of host rock and fault rock samples from the northern and southern shallow borehole sites. The methodologies of the transport property measurements are described in *Tanikawa et al*. [in press]. All samples for laboratory tests were cut and cored to cylindrical shapes that were 5 to 40 mm long and 20 mm in diameter. All experiments were performed in high-pressure apparatus at Kyoto University at room temperature under uniform (isostatic) confining pressure. All hydraulic properties were measured by using nitrogen gas as the pore fluid. Before testing, the samples were dried at 80 °C in an oven for a week to eliminate pore water without removing structural water adsorbed to clay mineral surfaces. We confined the samples using several polyolefin shrinkable jackets.

Permeability was measured by the steady-state gas flow method [*Wu et al.*, 1998] and the pore pressure oscillation method [*Kranz et al.*, 1990; *Fisher and Paterson*, 1992]. In the steady-state gas flow method, a differential pore pressure at a value between 0.2 and 2 MPa was applied across the sample and the pore pressure of downstream end was kept at a constant value of 0.1 MPa. In the oscillation method, we applied pore pressure of 20 MPa. The Klinkenberg effect [*Wu et al.*, 1998; *Tanikawa and Shimamoto*, 2008], which enhances gas permeability, may cause significant error in the conversion of gas permeability to water permeability, especially when gas permeability is measured at low pore pressure in low-permeability rocks. This phenomenon is attributed by ‘‘slip flow’’ between gas molecules and solid walls. Therefore, we transformed the measured gas permeability by the steady-state gas flow method to water permeability by using the Klinkenberg equation:

$$k_{gas} = k_w \left(1 + \frac{b}{\left(P_{up} + P_{down}\right)/2} \right), \qquad (2)$$

where k_w is the (intrinsic) permeability to water and b is the Klinkenberg factor, which depends on the pore structure of the medium and the temperature of the gas. Permeabilities of most of the core samples we used satisfied the Klinkenberg equation.

Porosity changes in response to confining pressure changes were determined by the gas expansion method [*Scheidegger*, 1974; *Wibberley*, 2002]. In this method, the volume of the saturated gas in pore spaces of the sample is measured by using the isothermal (Boyle-Mariotte) gas equations.

We calculated the drained pore compressibility from the results of the porosity test, and used this value for evaluation of specific storage [Wibberly, 2002]. The specific storage can also be evaluated by the pore pressure oscillation method, although the specific storage values thus obtained may contain significant errors, and vary by up to two orders of magnitude [*Takahashi and Kaneko*, 2003]. Therefore, only permeability was evaluated by the pore pressure-oscillation technique.

3. Results

3.1. Low-velocity Friction

The low-velocity friction response we observed was, in general, similar to that reported by previous works [e.g., *Dieterich,* 1979; *Marone,* 1998], though the friction coefficient and velocity dependence differed among gouges. Steady-state friction was achieved within 5 mm of slip distance, although in some experiments where we did not carry out cyclic shear loading at the beginning of the run (samples BAF057 and BAF062) friction increased slightly with increasing displacement (Figure 4a). Values of the friction coefficient for the dry northern fault gouge were twice those of wet gouge, indicating greater friction under dry than under wet conditions. In the gouge from the southern borehole, friction did not differ between dry and wet gouges even at different normal stress values (Figure 4b). Values of the steady-state friction coefficients in all tests were around 0.7. Notably, no displacement hardening was observed in any of the tests on the gouges. The friction coefficient of wet gouge also showed normal stress dependence, increasing as the applied normal stress was increased.

The northern fault gouge in most tests showed a positive velocity dependence of steady-state friction (Figure 4c). In contrast, the southern fault gouge showed velocity-weakening behavior (Figure 4d). We observed no remarkable relationship between velocity and the velocity dependence of steady-state friction. However, we observed a slight decrease in the velocity dependence of friction with increasing velocity for the northern fault gouge. Previous reports indicated a transition from velocity-strengthening to velocity weakening behavior [*Beeler et al.*, 1996; *Mair and Marone*, 1999], though we did not observe such a transition.

3.2. High-velocity Friction

In high-velocity friction tests, friction increased rapidly at the beginning of slip for all fault gouge samples, and then decreased gradually to a stable level. Peak values of the coefficient of friction were in the range of about 0.8 to 1.2, followed by a decrease to stable values between 0.2 and 0.3 (Figure 5). In most of the tests, values of the friction coefficients approached stable levels after 5 to 10 m of slip displacement. These frictional behaviors are similar to results obtained in previous high-velocity friction experiments for TCDP core samples and Nojima fault gouges associated with the 1995 Kobe earthquake [*Tanikawa et al.*, 2007; *Mizoguchi et al.,* 2007]. Both peak friction and steady-state friction decreased with increasing normal stress for the southern fault gouge. The amount of slip displacement that was necessary to achieve stable friction also decreased with increasing normal stress.

3.3. Permeability and Permeability Distribution

Cyclic effective pressure tests were performed on all host rock and fault rock specimens from the two shallow boreholes. Confining pressure was first increased from 0 to 200 MPa, and then decreased to 5 MPa. The results obtained for all of the transport property measurements are listed in Table 2 (only pressing path from 10 to 60 MPa is listed). In the northern core samples, initial permeability at 5 MPa ranged from 10^{-13} to 10^{-16} m^2, and permeability decreased as effective pressure increased (Figure 6a). The pressure sensitivity of permeability varied considerably among specimens. The permeable sandstones in Kueichulin Formation (NSA3- NSA5) showed very little sensitivity to effective pressure, and permeability decreased by less than one order of magnitude from the initial permeability, even at 200 MPa of effective pressure. In the other samples, permeability decreased by three to four orders of magnitude at the maximum effective pressure. The permeability of fault rocks (Fault gouge, Fault breccia) and siltstones decreased with depth. For all samples, the permeability change during unloading was much smaller than that during loading, and increased slightly at low effective pressure. Initial permeability was not fully recovered during unloading, even at the lowest effective pressure. The cyclic behavior of permeability in southern core samples (Figure 6b) was similar to that of the northern core samples. Gravels in the Toukoshan Formation showed higher permeability than fault rocks of Chinshui Shale origin. The lowest permeability was observed in fault breccias of Chinshui Shale at 156.5 m depth (SFF2), where it reached almost 10^{-20} m^2.

The permeability distributions at depths of 1, 2, and 3 km around the possible slip zones in the north and south shallow boreholes (FZ-B and FZ-C, Figure 7) were constructed by assuming that pore pressure is hydrostatic at depth and by applying a constant bulk density of 2500 kg/m^3. We assumed that the fault gouge at 305.5 m depth in the north borehole (NFG1) represents the gouge developed at 330 m depth in the same borehole. As we did not have the permeability data of the fault gouge at 330 m, we consider it to be analogous to that at 330m. As the relatively large proportions of clay minerals, which have developed as a result of shear deformation within the same thick fracture zone (285–330 m depth), are observed in the fault gouge at 305.5 m depth, we consider it to be analogous to that at 330m. In the northern shallow borehole, the permeability variation around the fault zone at 330 m depth, which possibly represents the 1999 Chi-Chi earthquake slip zone, is relatively small and varies within the range of one order of magnitude. The permeability around the southern fault zone is higher than that around the northern fault zone. Permeability in the footwall (Toukoshan Formation) is higher than that of the hanging wall, and the difference between footwall and hanging wall permeabilities is more than one order of magnitude (Figure 7b). Even though we lacked permeability data for the slip zone in the southern borehole, we considered that the permeability of the fault breccia at 173.5 m (SFF3) is representative of the permeability of the slip zone.

3.4. Porosity and Specific Storage

In core samples from the northern borehole, initial porosity ranged between 8% and 48%. As effective pressure increased to the maximum level tested, porosity decreased by 7% to 20% (Figure 8a). For all samples, the rate of porosity decrease became lower as effective pressure increased. Porosity partially recovered during unloading, but did not return to its initial value; this is similar to the pressure sensitive behavior of permeability discussed above. The porosity change was largest in the fault gouge at 305 m depth (NFG5) and smallest in the siltstone at 402.5 m depth (NSI5). The relationships of porosity to effective pressure for the southern borehole samples (Figure 8b) were similar to those of the northern borehole.

Initial values of specific storage in samples from the northern borehole ranged from 10^{-8} to 10^{-9} Pa^{-1}; and decreased rapidly by one order of magnitude with increasing effective pressure in most samples (Figure 8c). The pressure sensitivity of specific storage decreased as effective pressure increased and the shape of the curves was similar for all samples. The siltstone showed the smallest value of specific storage. This was around 10^{-10} Pa^{-1} at 200 MPa of effective pressure and was smaller than that of the other rocks. The relationships of specific storage to effective pressure for the southern core samples (Figure 8d) were similar to those of the northern borehole.

4. Thermal Pressurization Analysis

4.1 Numerical Modeling Parameters

We used the experimental data from the above investigations of frictional and transport properties for our thermal pressurization analysis. The mathematical model we used was based on those of previous studies [*Lachenbruch*, 1980; *Noda and Shimamoto*, 2005], which assume that one-dimensional diffusion of heat and fluid occurs normal to the fault plane. Temperature change is given by the sum of a heat production term and a heat transfer term [*Lachenbruch*, 1980] as follows:

$$\frac{\partial T}{\partial t} = \frac{A}{\rho c} + \frac{\kappa}{\rho c}\frac{\partial^2 T}{\partial x^2}, \qquad (3)$$

where t is time, x is distance normal to the fault from the center of the deformation zone, T is temperature rise, κ is thermal conductivity, ρ is bulk density, c is specific heat, and A is frictional heat generation per unit volume. All frictional work is assumed to convert to heat. The heat production rate A is given by

$$A = \tau \frac{V}{W}, \qquad (4)$$

where V is relative slip velocity during fault motion, W is width of the deformation zone, and τ is shear stress that can be described as

$$\tau = \mu_d (Pc - Pp), \qquad (5)$$

where μ_d is the dynamic friction coefficient, Pc is confining pressure, and Pp is pore pressure. Normal stress is assumed to be the same as overburden pressure. The change in pore pressure depends on the temperature change and Darcian fluid flux as follows:

$$\frac{\partial Pp}{\partial t} = \frac{\Phi \gamma}{Ss}\frac{\partial T}{\partial t} + \frac{1}{Ss}\frac{\partial}{\partial x}\left(\frac{k}{\eta}\frac{\partial Pp}{\partial x}\right), \qquad (6)$$

where γ is water expansibility, Ss is specific storage, k is permeability, η is water viscosity, and Φ is porosity. The physical and thermal properties we used for the numerical modeling are listed in Table 1. Thermal properties are from *Tanaka et al.* [2006a, 2006b], who measured thermal properties of the Chelungpu fault zone in the northern shallow borehole and the deep TCDP borehole. We assumed a thermal diffusivity of 1×10^{-6} m^2/s so that a value of the heat capacity C of 800 J/kg K is appropriate for our assumption of 2500 kg/m^3 for bulk density. In the modeling we used the same values for thermal properties for the northern and southern borehole data. Our experimental results showed that the transport properties of permeability, specific storage, and porosity changed as effective pressure changed, in a manner similar to that described by *Noda and Shimamoto* [2005]. Therefore, we described the transport properties as a function of effective pressure as proposed by *Noda and Shimamoto* [2005]. We also used different transport property values in the numerical modeling for the slip zone and the surrounding rocks; these values are shown in Figures 6 and 8.

Our friction tests showed that the friction coefficient decreased dramatically with slip distance at high velocity; this cannot be neglected in defining μ_d in equation (5) for the numerical modeling. The slip-weakening curve in our gouge experiments (Figure 5) is quite similar to previous results for fault gouge, which have been fitted by the following exponential equation [*Mizoguchi et al.*, 2007]:

$$\mu_d = \mu_r + (\mu_i - \mu_r)\exp\left(\frac{\ln(0.05)\cdot d}{d_c}\right), \tag{7}$$

where μ_r is residual coefficient of friction, μ_i is initial coefficient of friction, and d is displacement from initial coefficient of friction. We defined d_c as a specific displacement at which $\mu_i - \mu_r$ reduces to 5% of the initial value. When friction tests are conducted under dry conditions, the effect of pore pressure building up can be ignored in determining the value of μ_d. The friction parameters we used in our numerical modeling analyses are listed in Table 3. We assumed the slip velocity to be constant at 1 m/s for 10 s (i.e., 10 m of total slip displacement) in our analyses for both the northern and southern borehole sites. We also simplified the uniform strain rate distribution within the slip zone, such that the fault zone slips with the same slip velocity. We also assumed the same thickness of fault gouge (20 mm) at the northern and southern boreholes.

4.2 Numerical Modeling Results

Numerical modeling showed that the contrasting behavior of the northern and southern sections of the fault zone was because of differences in the degree of thermal pore fluid pressurization. The thermal pressurization mechanism was shown to be stronger at the northern borehole site than at the southern site. At the northern site, shear stress reduction was enhanced by increased pore pressure (Figure 9a and 9e). The thermal pressurization process was shown to have more effect at greater depths; the reduction of shear stress became much sharper with increasing depth. At the southern borehole site, shear stress was reduced only by the mechanical slip weakening described by equation (7), without additional stress reduction attributable to increased pore pressure at depth. This suggests that thermal pressurization was ineffective in the south. These contrasting behaviors reflect different temperature and pore pressure characteristics within the slip zone. For a given slip displacement, the temperature rise was smaller and pore pressure increase was larger in the north (Figure 9c). In contrast, the temperature rise was much larger in the south, and became considerably larger with increasing depth (Figure 9d). The numerical modeling analysis clearly showed that when the thermal pressurization process is eliminated, the rise of temperature is much stronger.

5. Discussion

Our experimental data and numerical modeling showed that low-velocity frictional behavior, transport properties, and the potency of the thermal pressurization mechanism differ in the northern and the southern sections of the Chelungpu fault. On the other hand, the behavior of fault gouge samples from the northern and southern sections of the fault under high-velocity friction was shown to be similar. This suggests that differences in physical properties along the fault likely influenced slip-weakening behavior and might have caused the contrasting slip behaviors observed in the northern and southern sections of the fault during the 1999 Chi-Chi earthquake.

The low-velocity frictional behavior of fault gouge from the northern and southern sections of the fault differed remarkably. Steady-state friction under wet conditions was generally higher in the southern gouge than in the northern gouge. Furthermore, we o observed velocity-strengthening behavior for the northern gouge, whereas tests on the southern gouge yielded velocity-weakening behavior. Fault instability in the south did not relate to wetness. The trends in low-velocity friction that we observed agree well with the results of previously reported simulated fault gouge experiments. *Kopf and Brown* [2003] reported that friction decreased with increasing clay mineral content. This is consistent with our observation that values of the friction coefficient for fault gouge from the southern borehole were higher than those of both the northern borehole. Clay content in the gouge of the southern borehole was lower than that in both the northern gouge. We also observed that friction in the quartz-rich southern fault gouge was independent of wetness, a result that is also consistent with previous work [*Frye and Marone,* 2002]. *Saffer et al*. [2001] found that the frictional velocity dependence ($a - b$)

of smectite shows normal stress dependence, and that the transition from velocity-weakening to velocity-strengthening occurs at around 30 MPa; these results are consistent with our findings for northern gouge under dry conditions. However, our results showed velocity-strengthening in the water-saturated northern under low normal stress. Our results agree with a previous study that showed that clay minerals become weaker with increasing water content, especially at high normal stress [*Ikari et al*., 2007]. Normal stress dependence of friction was more notable under wet conditions than under dry conditions in the northern fault gouge, and can be explained by the different water contents.

If we assume that the faulting mechanism of the 1999 Chi-chi earthquake is represented by the behavior of wet gouge, the velocity-weakening frictional behavior in the south is consistent with the onset of the seismicity of the earthquake. However, the northern gouge exhibits velocity-strengthening behavior, which implies stability; this is inconsistent with the large slip displacement and high velocity observed in the north during the 1999 Chi-Chi earthquake. This indicates that low-velocity friction properties are not applicable to the dynamic fault motions during the 1999 Chi-Chi earthquake.

It is plausible that a mechanism other than low-velocity friction controlled the slip dynamics that caused the large displacement in the north. Our experiments showed that high-velocity frictional behavior is very different from low-velocity frictional behavior, especially at the beginning of slip, when we observed a rapid decrease of shear stress. Furthermore, the steady-state values of the friction coefficient were much smaller in our high-velocity friction tests than in the low-velocity tests. The high-velocity frictional behavior in quartz-rich powdered gouge material is also different from that in solid rock [*Tsutsumi and Shimamoto*, 1997; *Hirose and Shimamoto*, 2005; *Hirose and Bystricky*, 2007]. Rock-on-rock friction in the low-velocity tests showed a much higher friction coefficient (0.4 to more than 0.6), though a rapid decrease of strength was commonly observed. The strength reduction might be associated with development of a molten layer, though in our gouge experiment we did not identify pseudotachylyte material and the temperatures reached were probably too low to melt the sample. Therefore, different concepts are needed to explain the low friction at high speed in the fault gouge.

Previously reported in situ temperature deficits [*Tanaka et al*., 2006a, 2006b; *Kano et al*., 2006] imply that dynamic friction was very low during the 1999 Chi-chi earthquake. They indicate that a friction coefficient as low as 0.05 to 0.12 is necessary to explain the heat deficit observed around the Chelungpu fault zone. In our low-velocity tests, we observed a high steady-state friction coefficient (a lowest value of 0.4) in all fault gouges, even under wet conditions. In contrast, the high-velocity steady-state value of the friction coefficient was very low, only 0.2, a similar value to that of the crushed gouge obtained from the deep borehole penetrating the Chelungpu fault [*Tanikawa et al*., 2007]. If these low friction values can be extrapolated to depth (though the high-velocity tests were carried at very low normal stress), we can reasonably explain the observed temperature anomaly.

We observed no remarkable difference in high-velocity frictional behavior of the northern and the southern gouges. On the other hand, our numerical modeling of the thermal pressurization weakening mechanism showed that thermal pressurization probably occurred along the northern section of the fault, but not along the southern section of the fault. In our modeling, the thermal properties, slip zone width, and slip velocity we used were the same in the north and south, so the different degrees of thermal pressurization along the fault were likely caused by stratigraphically controlled hydrological variations in the fault zone. In the south, the slip zone is at the stratigraphic boundary between the permeable Toukoshan Formation and the Chinshui Shale. In the north, however, slip occurred within the impermeable Chinshui Shale. This structural contrast of the Chelungpu fault can be extrapolated to at least 3 to 4 km depth [*Yue et al.*, 2005], which explains the relatively lower permeability of the northern fault zone. Thermal pressurization not only enhances the decrease of stress but also increases fault instability according to the value of D_C, as follows [*Mikumo et al.*, 2003; *Wibberley and Shimamoto*, 2005]. For similar decreases of fault strength, a fault would be less stable for smaller values of *Dc*. This is because instabilities arise from a force imbalance if the fault weakens at a faster rate during rupture than the decrease of driving shear stress in the surrounding medium. Hence, the enhancement of stress release and increased fault instability during dynamic slip as a result of thermal pressurization may explain the greater slip displacement in the northern Chelungpu fault zone.

Recent studies have proposed other possible dynamic weakening mechanisms. The lack of microscopic evidence for melting [*Hirono et al*., 2006] suggests that melt lubrication [*Hirose and Shimamoto*, 2005] was not the main dynamic weakening mechanism for the northern fault zone. *Ma et al*. [2003] suggested that dynamic weakening in the north may have been caused by a hydrodynamic lubrication mechanism [*Brodsky and Kanamori*, 2001], but did not provide mechanical or physical data for fault gouge material to support their assertion. Chemical reactions caused by thermal decomposition are another possible weakening mechanism [*Han et al.*, 2007], as several chemical anomalies associated with heating have been observed in the Chelungpu fault [*Hirono et al.*, 2006; *Mishima et al.*, 2006]. However, the likelihood of this is low because the fault rocks are composed mainly of quartz and feldspar, and lack the minerals that are commonly involved in thermal decomposition. When flash weakening [*Rice*, 2006; *Beeler et al.*, 2008] occurs at microscopic asperity contacts on a fault, where very high temperatures are generated at very short-lived contacts, it results in a dramatic reduction in shear strength due to melting or phase transition at asperity contacts. We observed magnetic susceptibility change of gouge samples (Table 3) and partial gel formations of Teflon at lateral of cylindrical samples after high-velocity friction tests, suggesting a moderate temperature increase at the slip surface. Magnetic property change of the fault rocks in the Chelungpu Fault was well studied [*Mishima et al.*, 2006; *Tanikawa et al.*, 2007], and the magnetic susceptibility change suggests temperature within the fault gouge was raised at least 400°C due to frictional heating, which is consistent with the melting of Teflon jacket (melting point is 327 °C) . High-velocity friction tests were performed at dry condition, where thermal pressurization mechanism is neglected, therefore the large dynamic stress drop observed in high-velocity friction tests can be explained by flash weakening model. The slip rates of the Chelungpu Fault and high-velocity friction tests are large enough to cause dynamic weakening by flash heating [*Beeler et al.*, 2008], whereas the large slip weakening distances observed in both the seismic data [*Zhang et al.*, 2003] and friction tests (several m) are inconsistent with flash heating model. Therefore flash weakening model is not enough to satisfy the slip behavior of the Chelungpu Fault.

We assumed 20 mm thickness of deformation zone for the thermal pressurization analysis, though it is, in general, difficult to define the deformation thickness accurately. 7 mm thickness of the fault gouge layer was observed at the FZ-B and 1 mm thick dark gray layer was observed at the FZ-C in the north shallow borehole [*Tanaka et al.*, 2002], though blackish ultracataclasite layers 10 to 20 mm thick are developed in the center of fault zones at the TCDP deep borehole [*Hirono et al.*, 2006]. Therefore thickness of the slip zone of the Chelungpu Fault can be in the range of several mm to several ten mm. If the thickness of shear zone is within the range of 5 to 100 mm, the contrasting slip behavior that thermal pressurization is relatively effective in the north and ineffective in the south is still acceptable (Figure 10).

It is not certain that the low-velocity friction behavior evaluated using the shallow borehole samples represent the friction behavior at the hypocentral depth of the Chi-Chi earthquake (8-10 km) [*Chang et al.*, 2000; *Kuo et al.*, 2000]. Assuming a liner temperature gradient (22-30 °C/km) [*Suppe and Wittke*, 1977; *Kano et al.*, 2006] and a hydrostatic stress, the temperature and the vertical stress at the hypocentral depth are estimated to be 200-300 °C and 120-150 MPa, respectively. Therefore, thermally driven mineral transitions, such as dehydration of smectite to illite and dehydroxidation of kaolinite, can occur in the fault zone at depth. In the western Taiwan basin, the transition depth from smectite to illite is assumed to be around 4 km [*Tanikawa et al.*, in press], therefore, illite-rich gouges are expected in the northern fault zone at the hypocentral depth. On the other hand, the dominant composition of the fault gouge may not change in the southern gouge because the fault gouge is mainly composed of quartz. Even if the transformation of smectite to illite occurs at a depth of fault zones, the stable slip behavior is expected, because illite-rich gouge shows only velocity-strengthening behavior over the entire range of normal stress [*Saffer and Marone*, 2003]. Therefore, the contrasting velocity-dependent frictional behavior between the northern and the southern fault rocks is expected at the hypcentral depth, on the assumption that the variation of the relative proportion of clay and quartz within the fault zone, which is observed at shallow borehole samples, is preserved at the hypocentral depth.

6. Conclusions

The behavior of fault gouge materials from shallow boreholes on the Chelungpu fault during high-velocity slip is much different than during low-velocity slip. At high slip rates, a rapid reduction of friction was observed immediately after the onset of slip. We found the behavior of northern and southern gouge was similar during high-velocity slip. In contrast, permeability distributions showed differences between the north and south. Even though specific storage values were similar, permeability was shown to be one order of magnitude smaller in the north than in the south. Thermal pressurization modeling using the measured frictional and transport properties indicated that thermal pressurization was relatively effective in the north, where dynamic stress reduction was enhanced by an increase of pore pressure due to frictional heating. In contrast, thermal pressurization was ineffective in the south. The contrasting slip behavior between north and south is, therefore, explained by the effectiveness of fault weakening due to thermal pressurization.

Assuming that the behavior of wet gouge under low-velocity friction is representative of the faulting mechanism, the velocity-weakening friction behavior in the south is consistent with nucleation of the 1999 Chi-Chi earthquake. The probable low friction during the slip event, as estimated from in situ temperature measurements, can be explained by the occurrence of thermal pressurization during the earthquake and dramatic fault weakening during high-velocity slip in the north.

Acknowledgments

We thank M. Ando, H. Tanaka, C. Y. Wang, and their colleagues for their efforts in planning and completing shallow drilling on the Chelungpu fault, and for making the core samples available for our study. We are greatly appreciated to H. Noda for supporting the numerical analysis. We really appreciate thoughtful suggestions from the associate editor and the anonymous reviewers. We also thank W. M. Chen and C. W. Lin for extensive support of the work in Taiwan.

References

Beeler, N. M., T. E. Tullis, M. L. Blanpied, and J. D. Weeks (1996), Frictional behavior of large displacement experimental faults, *J. Geophys. Res.*, *101*, (B4), 8697–8715.

Beeler, N. M., T. E. Tullis, and D. L. Goldsby (2008), Constitutive relationships and physical basis of fault strength due to flash heating, *J. Geophys. Res. 113*, B01401, doi:10.1029/2007JB004988.Brodsky, E., and H. Kanamori (2001), Elastohydrodynamic lubrication of faults, *J. Geophys. Res.*, *106*, 16357–16374.

Chang, C. H., Y. M., Wu, T. C., Shin, C. Y. Wang (2000), Relocation of the 1999 Chi-Chi Earthquake in Taiwan, *Terr. Atmos. Oceanic Sci.*, *11*, 581–590.

Dieterich, J. H. (1978), Time-dependent friction and the mechanics of stick slip, *Pure Appl. Geophys.*, 116, 790–806.

Dieterich, J. H. (1979), Modeling of rock friction, 1. Experimental results and constitutive equations, *J. Geophys. Res*., *84*, 2161–2168.

DiToro, G., D. L. Goldsby, and T. E. Tullis (2004), Friction falls towards zero in quartz rock as slip velocity approaches seismic rates, *Nature*, *427*, 436– 439.

Fischer, G. J., and M. S. Paterson (1992), Measurement of permeability and storage capacity in rocks during deformation at high temperature and pressure, in *Fault mechanics and transport properties of rocks,* edited by B. Evans, and T. F. Wong, pp. 187–211, Academic Press, London.

Frye, K. M., and C. Marone (2002), Effect of humidity on granular friction at room temperature, *J. Geophys. Res*., *107*, B11, 2309, doi:10.1029/2001JB000654.

Han, R., T. Shimamoto, T. Hirose, J.-H. Ree, and J. Ando (2007), Ultra-low friction of carbonate faults caused by thermal decomposition, *Science*, 316, 878–881.

Hashimoto, Y., K. Ujiie, A. Sakaguchi, and H. Tanaka, (2007), Characteristics and implication of clay minerals in the northern and southern parts of the Chelung-pu fault, Taiwan, *Tectonophysics*, *443*, 233-242.

Hirono, T., M. Ikehara, K. Otsuki, T. Mishima, M. Sakaguchi, W. Soh, M. Omori, W. Lin, E.-C. Yeh, W. Tanikawa, and C.-Y. Wang (2006), Evidence of frictional melting from disk-shaped black material, discovered within the Taiwan Chelungpu fault system, *Geophys. Res. Lett.*, *33*, L19311, doi:10.1029/2006GL027329.

Hirono, T., K. Fujimoto, T. Yokoyama, Y. Hamada, W. Tanikawa, O. Tadai, T. Mishima, M. Tanimizu, W. Lin, W. Soh, and S.-R. Song (2008), Clay mineral reactions caused by frictional heating during an earthquake: An example from the Taiwan Chelungpu fault, *Geophys. Res. Lett.*, 35, L16303, doi:10.1029/2008GL034476.

Hirose, T., and T. Shimamoto (2005), Growth of molten zone as a mechanism of slip weakening of simulated faults in gabbro during frictional melting, *J. Geophys. Res., 110*, B05202, doi:10.1029/2004JB003207.

Hirose. T., and M. Bystricky, (2007), Extreme dynamic weakening of faults during dehydration by coseismic shear heating, *Geophys. Res. Lett.*. *34*, L14311, doi:10.1029/2007GL030049.

Huang, C. S., K. S. Shea, and M. M. Chen (2000),The geologic map of Taiwan, Puli Sheet, Taipei, Central geological survey of Taiwan, 32, 1:50,000.

Huang, S. T., J. C. Wu, J. H. Hung, and H. Tanaka (2002), Studies of sedimentary facies, stratigraphy, and deformation structures of the Chelungpu fault zone on cores from drilled wells in Fengyuan and Nantou, Central Taiwan, *Terr. Atmos. Oceanic Sci.*, *13*, 253–278.

Ikari, M. J., D. M. Saffer, and C. Marone (2007), Effect of hydration state on the frictional properties of montmorillonite-based fault gouge, *J. Geophys. Res.*, *112*, B06423, doi:10.1029/2006JB004748.

Kano, Y., J. Mori, R. Fujio, H. Ito, T. Yanagidani, S. Nakao, and K. F. Ma (2006), Heat signature on the Chelungpu fault associated with the 1999 Chi-Chi, Taiwan Earthquake, *Geophys. Res. Lett.*, *33*, L14306, doi:10.1029/2006GL026733.

Kawamoto, E., and T. Shimamoto (1998), The strength profile for bimineralic shear zones, an insight from high-temperature shearing experiments on calcite–halite mixtures, *Tectonophysics*, 295,1-14.

Kranz, R. L., J. S. Saltzman, and J. D. Blacic (1990), Hydraulic diffusivity measurements on laboratory rock samples using an oscillating pore pressure method, *International Journal of Rock Mechanics and Mining Sciences and Geomechanics Abstracts*, 27, 5, 345–352.

Kopf, A., and K. M. Brown (2003), Friction experiments on saturated sediments and their implications for the stress state of the Nankai and Barbados subduction thrusts, *Mar. Geol.*, *202*, 193–210.

Kao, H., R. Y. Chen, and C. H. Chang (2000), Exactly where does the 1999 Chi-Chi earthquake in Taiwan nuclear?—Hypocenter relocation using the master station method. *Terr. Atmos. Ocean. Sci.*, **11**, 567-580.

Lachenbruch, A. (1980), Frictional heating, fluid pressure, and the resistance to fault motion, *J. Geophys. Res.*, *85*, 6097–6112.

Lee, J. C., H. T. Chu, J. Angelier, Y. C. Chan, J. C. Hu, C. Y. Lu, and R. J. Rau (2002), Geometry and structure of northern surface ruptures of the 1999 Mw = 7.6 Chi-Chi Taiwan earthquake: Influence from inherited fold belt structures, *J. Struct. Geol.*, *24*, 173– 192.Lo, W., L. C. Wu, and H. W. Chen (1999),The geologic map of Taiwan, Kouhsing Sheet, Taipei, Central geological survey of Taiwan, 25, 1:50,000.

Luo, X., and G. Vasseur (1992), Contribution of compaction and aquathermal pressuring to geopressure and the influence of environmental conditions, *AAPG Bull, 76,* 1550–1559.

Ma, K. F., T. R. A. Song, S. J. Lee, and H. I. Wu (2000), Spatial slip distribution of the September 20, 1999, Chi-Chi Taiwan, Earthquake (Mw7.6)—Inverted from teleseismic data, *Geophys. Res. Lett.*, *27*(20), 3417-3420.

Ma, K., E. E. Brodsky, J. Mori, C. Ji, T. A. Song, and H. Kanamori (2003), Evidence for fault lubrication during the 1999 Chi-Chi, Taiwan, earthquake (Mw7.6), *Geophys. Res. Lett.*, *30*(5), 1244, doi:10.1029/2002GL015380.

Mair, K., and C. Marone (1999), Friction of simulated fault gouge for a wide range of velocities and normal stresses, *J. Geophys. Res*., *104*, (B12), 28899–28914.

Marone, C. (1998), Laboratory-derived friction laws and their application to seismic faulting, *Ann. Rev. Earth Planet. Sci.*, *26*, 643–696.

Mikumo, T., K. B. Olsen, E. Fukuyama, and Y. Yagi (2003), Stress-breakdown time and slip-weakening distance inferred from slip-velocity functions on earthquake faults, *Bull. Seismol. Soc. Am. 93*, 264–282.

Mishima, T., H. Hirono, W. Soh, and S.-R. Song (2006), Thermal history estimation of the Taiwan Chelungpu fault using rock-magnetic methods, *Geophys. Res. Lett.*, *33*, L23311, doi:10.1029/2006GL028088.

Mizoguchi, K., T. Hirose, T. Shimamoto, and E. Fukuyama (2007), Reconstruction of seismic faulting by high-velocity friction experiments: An example of the 1995 Kobe earthquake, *Geophys. Res. Lett.*, *34*, L01308, doi:10.1029/2006GL027931.

Mouthereau, F., B. Deffontaines, O. Lacombe, and J. Angelier (2002), Variations along the strike of the Taiwan Thrust belt; basement control on structural style, wedge geometry, and kinematics, *Geological Society of America Special Paper*, *385*, 31–54.

Neuzil, C. E. (1994), How permeable are clays and shales?, *Water Resources Research*, *30*, 145–150.

Noda, H., and T. Shimamoto (2005), Thermal pressurization and slip-weakening distance of a fault: An example of the Hanaore fault, Southwest Japan, *Bulletin of the Seismological Society of America*, *95*, 1224–1233.

Otsuki, K., and N. Monzawa (2001), Contrasting fault rocks from two boreholes penetrating Chelungpu fault, Taiwan, *Proceedings of ICDP Workshop on Drilling the Chelungpu fault*, Taiwan, 90–92.

Rice, J. R, and A. Ruina (1983), Stability of steady frictional sliding, *J. Appl. Mech.*, *105*, 343-349.

Rice, J. R. (2006), Heating and weakening of faults during earthquake slip, *J. Geophys. Res., 111*, B05311, doi:10.1029/2005JB004006.

Saffer, D., M. K. M. Frye, C. Marone, and K. Mair (2001), Laboratory results indicating complex and potentially unstable frictional behaviors of smectite clay, *Geophys. Res. Lett.*, *28*(12), 2297–2300.

Saffer, D. M., and C. Marone (2003), Comparison of smectite- and illite-rich gouge frictional properties: Application to the updip limit of the seismogenic zone along subduction megathrusts, *Earth Planet. Sci. Lett., 215*, 219– 235.

Scheidegger, A. E. (1974), *The physics of flow through porous media*, 3rd ed., 102 pp., University of Toronto Press, Toronto.

Shimamoto, T., and A. Tsutsumi (1994), A new rotary-shear high-speed frictional testing machine: Its basic design and scope of research (in Japanese with English abstract), *J. Tecton. Res. Group Jpn.*, *39*, 65–78.

Shin, T. C., and T. Teng (2001), An Overview of the 1999 Chi-Chi, Taiwan, Earthquake, *Bulletin of the Seismological Society of America*, *91*, 5, 895–913.

Sibson, R. H. (1973), Interactions between temperature and pore fluid pressure during an earthquake faulting and a mechanism for partial or total stress relief, *Nature*, 243, 66–68.

Suppe, J., and J. H. Wittke (1977), Abnormal pore-fluid pressures in relation to stratigraphy and structure in the active fold-and-thrust belt of northwestern Taiwan, *Petroleum Geology of Taiwan, 14,* 11–24.

Takahashi, M., and T. Kaneko (2003), Permeability measurements using oscillation method and an application for deformed rock specimen (in Japanese with English abstract), *Shigen-to-Sozai*, *119*, 501–507.

Tanaka, H., C. Y. Wang, W. M. Chen, A. Sakaguchi, K. Ujiie, H. Ito, and M. Ando (2002), Initial science report of shallow drilling penetrating into the Chelungpu fault zone, Taiwan, *Terr. Atmos. Oceanic Sci.*, *13*, 227–251.

Tanaka, H., W. M. Chen, C. Y. Wang, K. F. Ma, N. Urata, J. Mori, and M. Ando (2006a), Frictional heat from faulting of the 1999 Chi-Chi, Taiwan earthquake, *Geophys. Res. Lett.*, *33*, L16316, doi:10.1029/2006GL026673.

Tanaka, H., W. M. Chen, K. Kawabata, and N. Urata (2006b), Thermal properties across the Chelungpu fault zone and evaluations of positive thermal anomaly on the slip zones: Are these residuals of heat from faulting?, *Geophys. Res. Lett.*, *34*, L01309, doi:10.1029/2006GL028153.

Tanikawa, W., T. Mishima, T. Hirono, W. Lin, T. Shimamoto, W. Soh, and S. Song, (2007), High magnetic susceptibility produced in frictional tests on core samples from the Chelungpu fault in Taiwan. *Geophys. Res. Lett.*, *34*, L15304, doi:10.1029/2007GL030783

Tanikawa W., T. Shimamoto (2008), Comparison of Klinkenberg-corrected gas permeability and water permeability in sedimentary rocks, *International Journal of Rock Mechanics & Mining Sciences*.

Tanikawa, W., T, Shimamoto, S.-K. Wey, C.-W. Lin, W.-C. Lai (in press), Stratigraphic variation of transport properties and overpressure development in the Western Foothills, Taiwan. *J. Geophys. Res.*

Tsutsumi, A., and T. Shimamoto (1997), High-velocity frictional properties of gabbro, *Geophys. Res. Lett.*, *24*, 699–702.

Wang, C. Y., C. H. Chang, and H. Y. Yen (2000), An interpretation of the 1999 Chichi earthquake, in Taiwan based on the thin-skinned thrust model, *Terr. Atmos. Oceanic Sci.*, *13*, 153–170.

Wang, C. Y., C. L. Li, F. C. Su, M. T. Leu, M. S. Wu, S. H. Lai, and C. C.Chern (2002), Structural mapping of the 1999 Chi-Chi earthquake fault, Taiwan by seismic reflection methods. *Terr. Atmos. Oceanic Sci.*, *13*, 211–226.

Wibberley, C. (2002), Hydraulic diffusivity of fault gouge zones and implications for thermal pressurization during seismic slip, *Earth Planets Space, 54,* 1153–1171.

Wibberley, C. A. J., and T. Shimamoto (2005), Earthquake slip weakening and asperities explained by thermal pressurization, *Nature*, *436*, 689–692.

Wu, Y. S., K. Pruess, and P. Persoff (1998), Gas flow in porous media with Klinkenberg's effect, *Transport in Porous Media*, *32*, 117–137.

Yue, L. F., J. Suppe, and J. H. Hung (2005), Structural geology of a classic thrust belt earthquake: the 1999 Chi-Chi earthquake Taiwan (M_w=7.6), *Journal of Structural Geology*, *27*, 2058–2083.

Zhang, W., T. Iwata, and K. Irikura (2003), Heterogeneous distribution of the dynamic source parameters of the 1999 Chi-Chi, Taiwan, earthquake, *J. Geophys. Res.*, *108*, B5, 2232, doi:10.1029/2002JB001889.

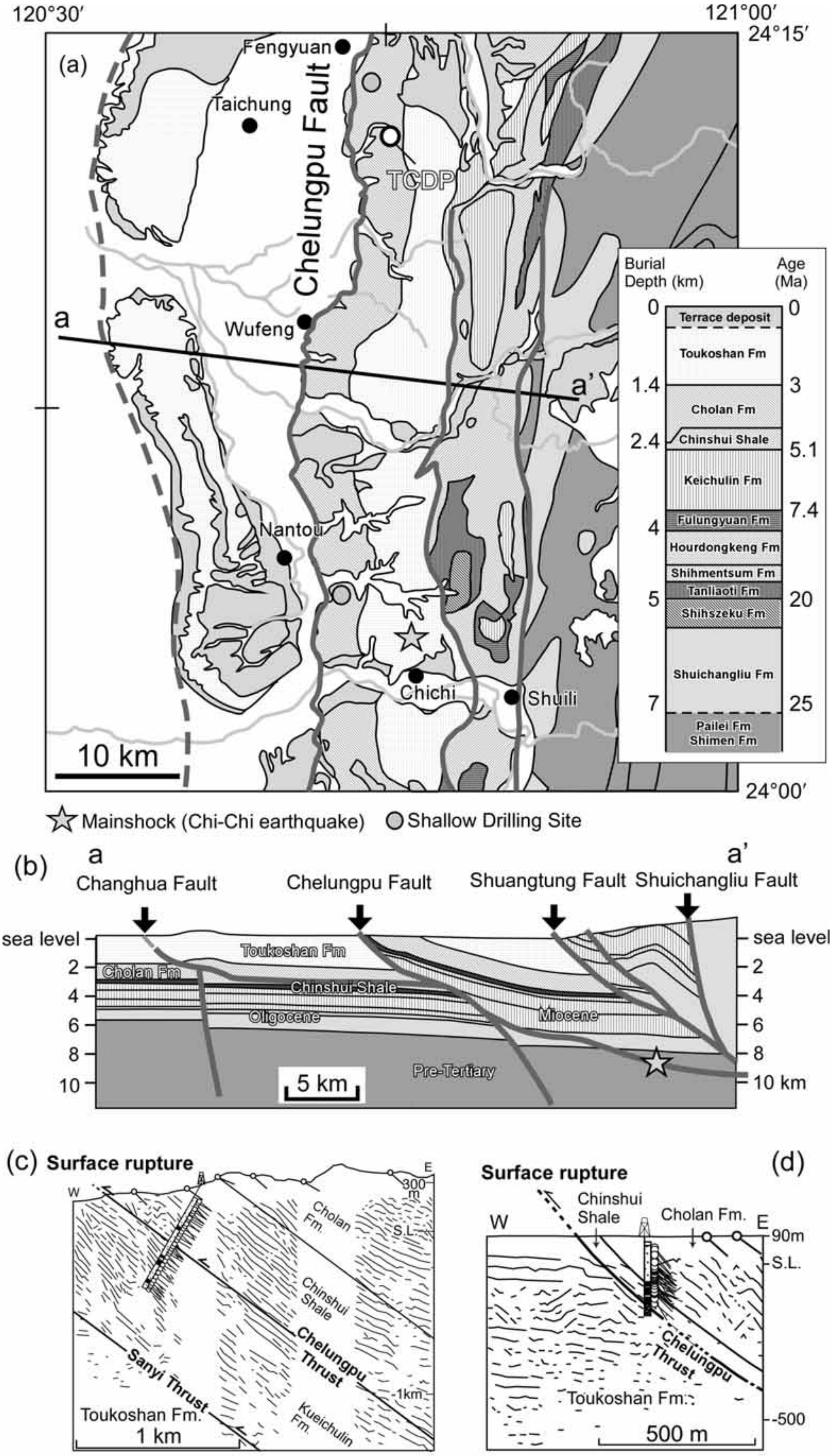
120°30′
121°00′
24°15′
24°00′
(a)
Fengyuan
Taichung
Chelungpu Fault
TCDP
Wufeng
Nantou
Chichi
Shuili
a
a′
10 km
Burial Depth (km)
Age (Ma)
Terrace deposit
Toukoshan Fm
Cholan Fm
Chinshui Shale
Keichulin Fm
Fulungyuan Fm
Hourdongkeng Fm
Shihmentsum Fm
Tanliaoti Fm
Shihszeku Fm
Shuichangliu Fm
Pailei Fm
Shimen Fm
Mainshock (Chi-Chi earthquake)
Shallow Drilling Site
(b)
Changhua Fault
Chelungpu Fault
Shuangtung Fault
Shuichangliu Fault
sea level
Toukoshan Fm
Cholan Fm
Chinshui Shale
Oligocene
Miocene
Pre-Tertiary
5 km
10 km
(c)
Surface rupture
W
E
300 m
Cholan Fm.
Chinshui Shale
S.L.
Chelungpu Thrust
Sanyi Thrust
Kueichulin Fm.
-1km
Toukoshan Fm.
1 km
(d)
Surface rupture
Chinshui Shale
Cholan Fm.
W
E
90m
S.L.
Chelungpu Thrust
Toukoshan Fm.
-500
500 m

Figure 1. (a) Geological map and geological column of the study area (after *Lo et al.*, 1999; *Huang et al.*, 2000; *Wang et al.*, 2000) showing locations of the northern (Fengyuan) and southern (Nantou) shallow drilling sites, and the deep TCDP drillhole. (b) Geological cross section through the area affected by the 1999 Chi-Chi earthquake (after *Mouthereau et al.*, 2002). The location of the mainshock is shown by a star. (c) Geological interpretation of a shallow reflection seismic section at the northern borehole site. (d) Geological interpretation of a shallow reflection seismic section at the southern borehole site (modified from *Wang et al.*, 2002 and *Yue et al.*, 2005). Seismic data interpretation was correlated with shallow borehole data and surface dip measurements.

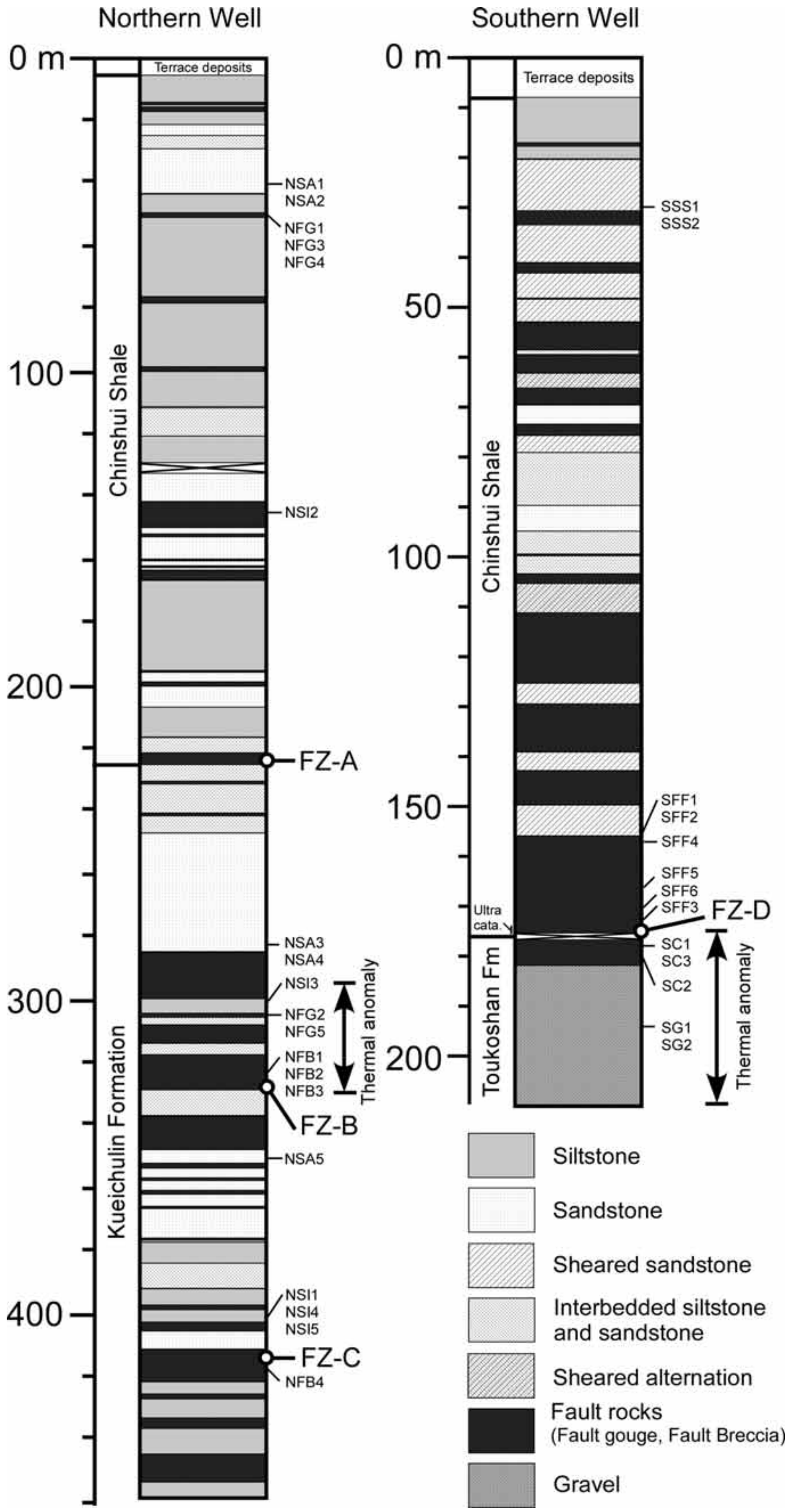

Northern Well
Southern Well
0 m
100
200
300
400
50
150
Terrace deposits
Chinshui Shale
Kueichulin Formation
Toukoshan Fm
NSA1
NSA2
NFG1
NFG3
NFG4
NSI2
FZ-A
NSA3
NSA4
NSI3
NFG2
NFG5
NFB1
NFB2
NFB3
FZ-B
NSA5
NSI1
NSI4
NSI5
FZ-C
NFB4
Thermal anomaly
SSS1
SSS2
SFF1
SFF2
SFF4
SFF5
SFF6
SFF3
FZ-D
Ultra cata.
SC1
SC3
SC2
SG1
SG2
Siltstone
Sandstone
Sheared sandstone
Interbedded siltstone and sandstone
Sheared alternation
Fault rocks (Fault gouge, Fault Breccia)
Gravel

Figure 2. Lithologic columnar sections of northern (Fengyuan) and southern (Nantou) wells (Huang et al., 2002;Tanaka et al, 2002) and sample location. FZ-A to FZ-D indicate the candidate fault zones related to the Chi-Chi earthquake.

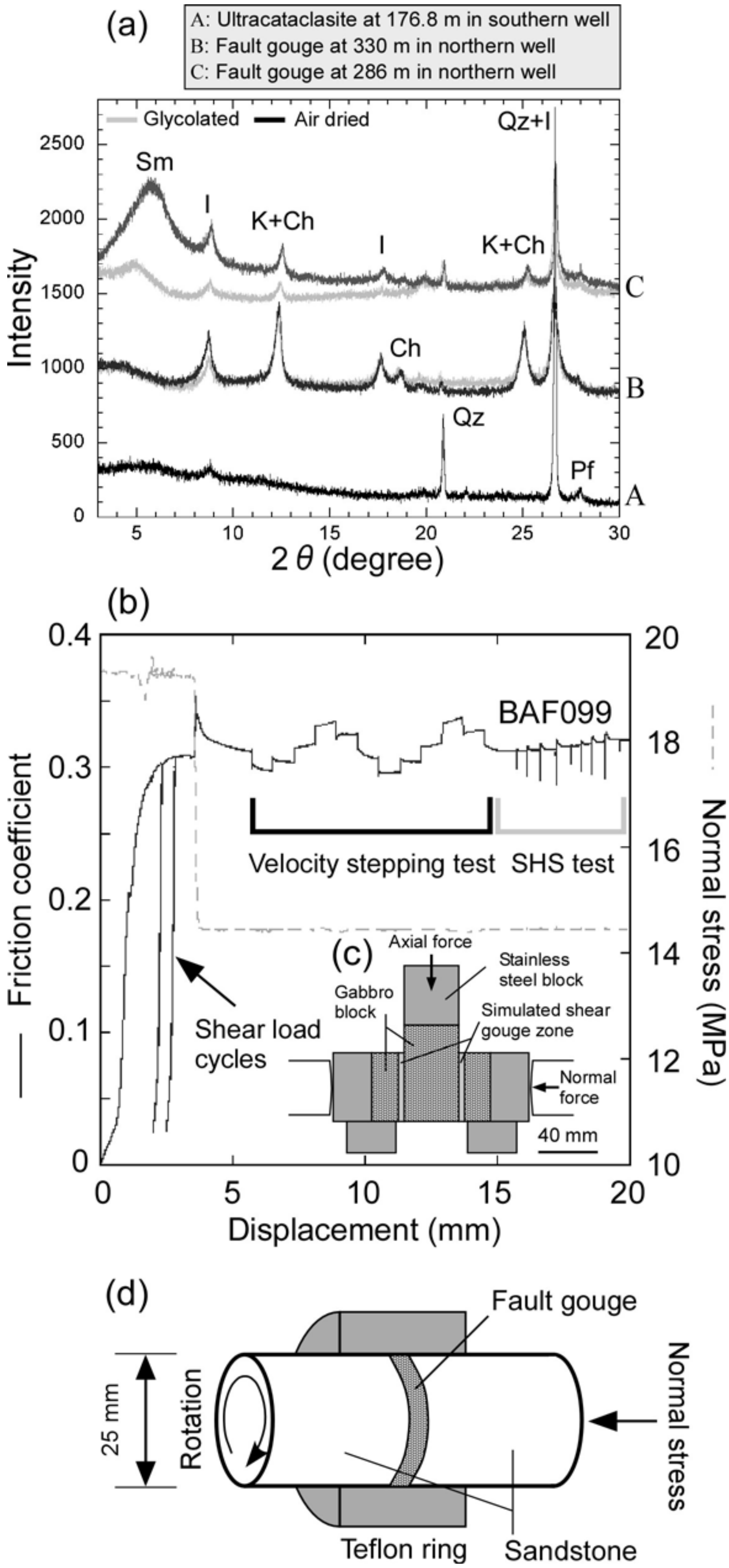

Figure 3. (a) XRD patterns from oriented, glycolated and air-dried fault gouge samples

used in the double-layered low-velocity experiments. Sm, smectite; Ch, chlorite; I, illite; K, kaolinite; Qz, quartz; Pf, potassium feldspar. (b) Shear stress and normal stress history of one experimental set. Before the velocity-stepping tests, gouge layers were subjected to two shear-load cycles at high normal stress (19 MPa) to create a fresh surface area. Slide-hold-slide (SHS) tests were carried out at a normal stress of 14 MPa. (c) Schematic diagram of the apparatus used for the biaxial low-velocity friction tests. (d) Schematic diagram of the apparatus used for the high-velocity rotation (HVR) friction tests.

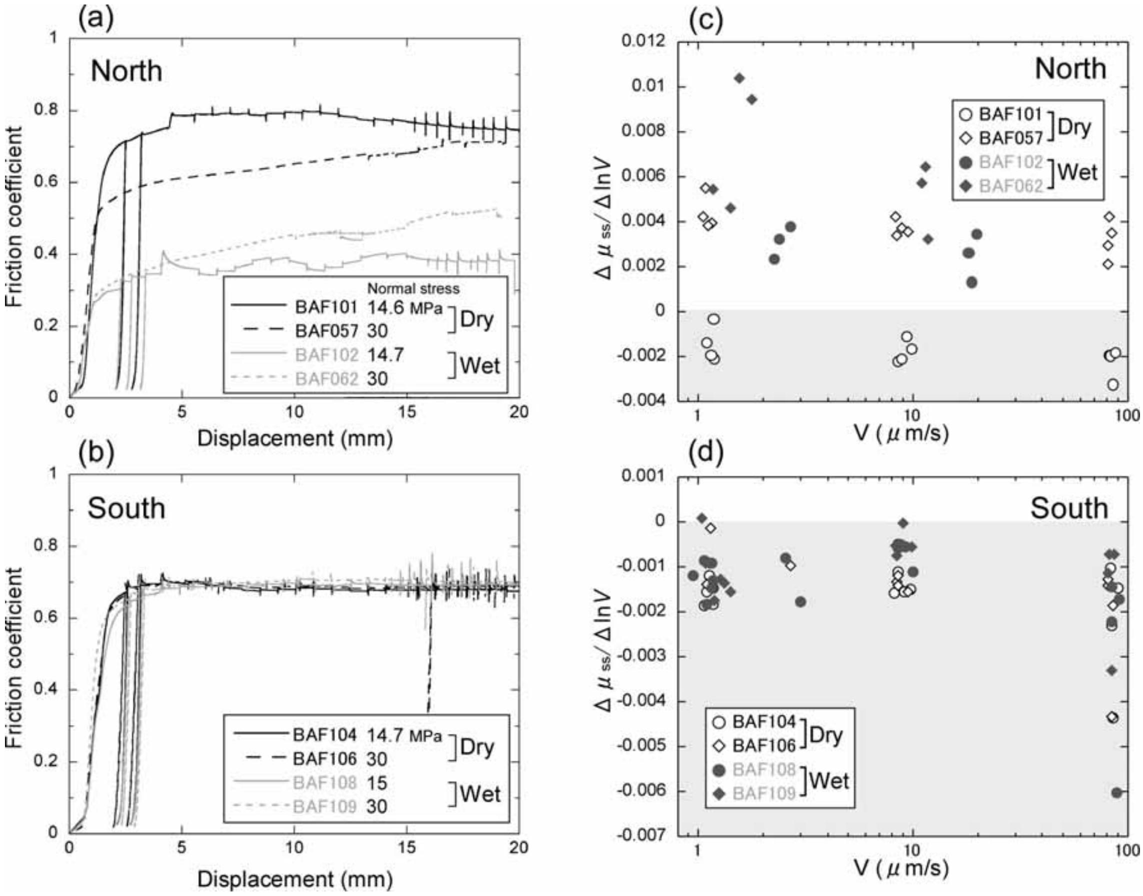

Figure 4. Friction coefficient vs. displacement curves under various conditions of normal stress and relative humidity for fault gouges from (a) the northern borehole, and (b) the southern borehole. (c) and (d) velocity dependence of steady-state friction as a function of velocity for the same fault rocks shown in Figure 3a, and b.

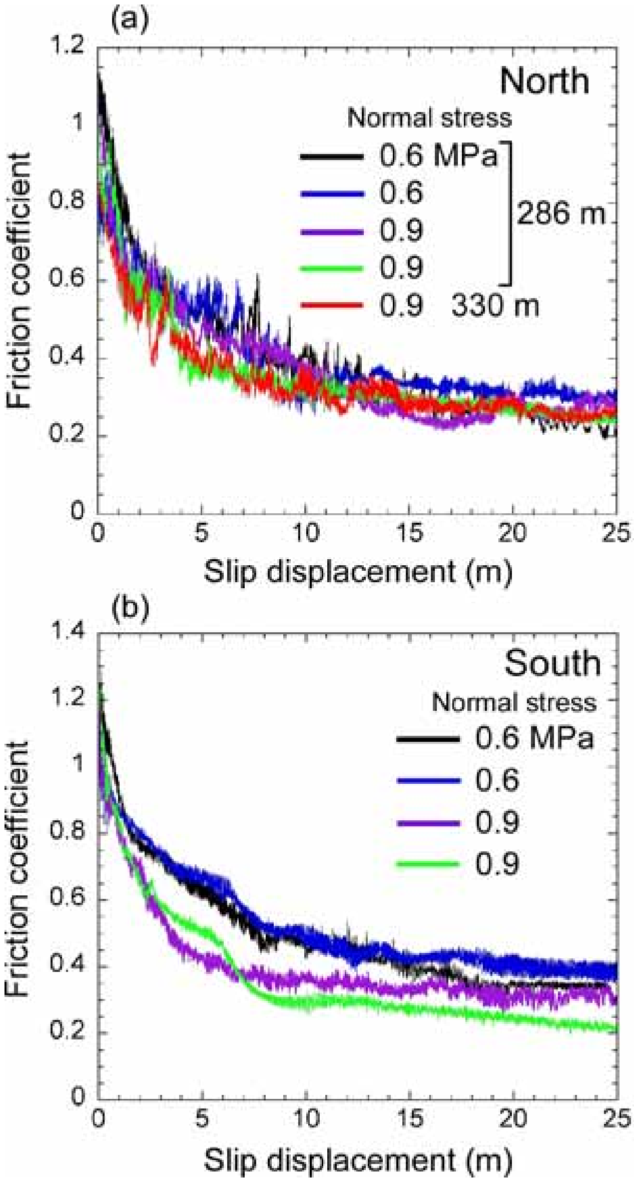

Figure 5. Friction as a function of slip displacement for the high-velocity friction tests of fault gouge samples at various normal stress levels and a constant equivalent slip velocity of 1.03 m/s. Fault gouges from (a) the northern borehole, and (b) the southern borehole.

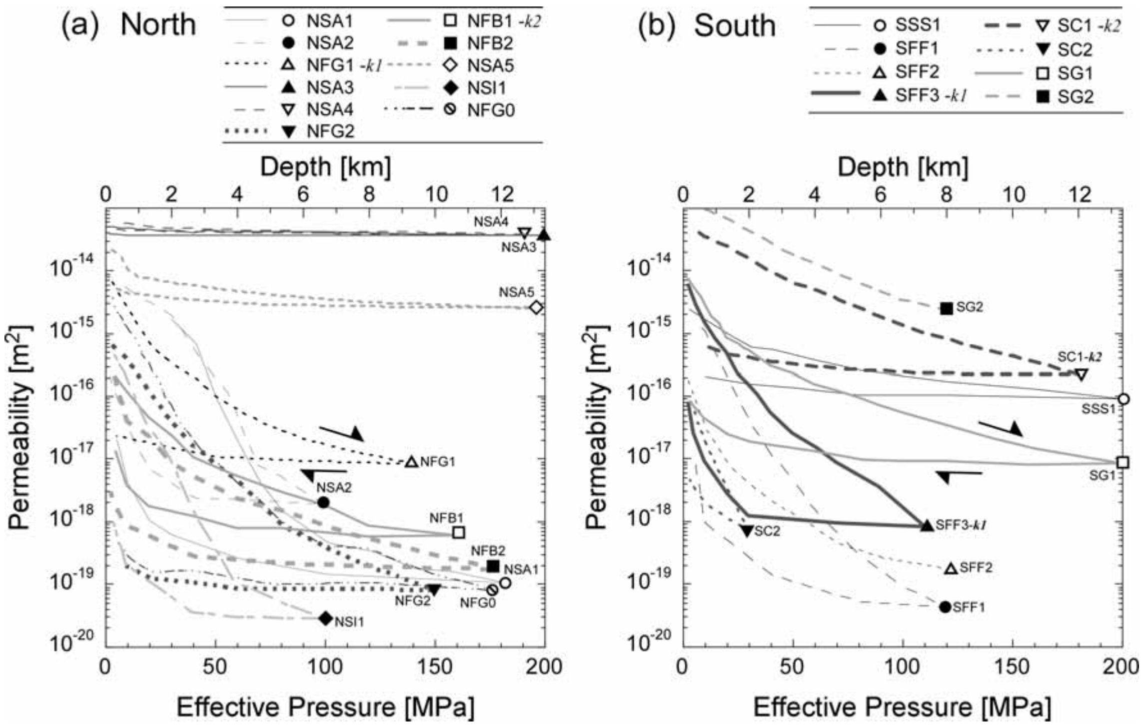

Figure 6. Permeability as a function of effective pressure during one pressure cycling test for (a) the northern, and (b) the southern shallow borehole samples. *k1* and *k2* are the permeabilities of the slip zone and the surrounding rock, respectively, which were used for thermal pressurization analysis.

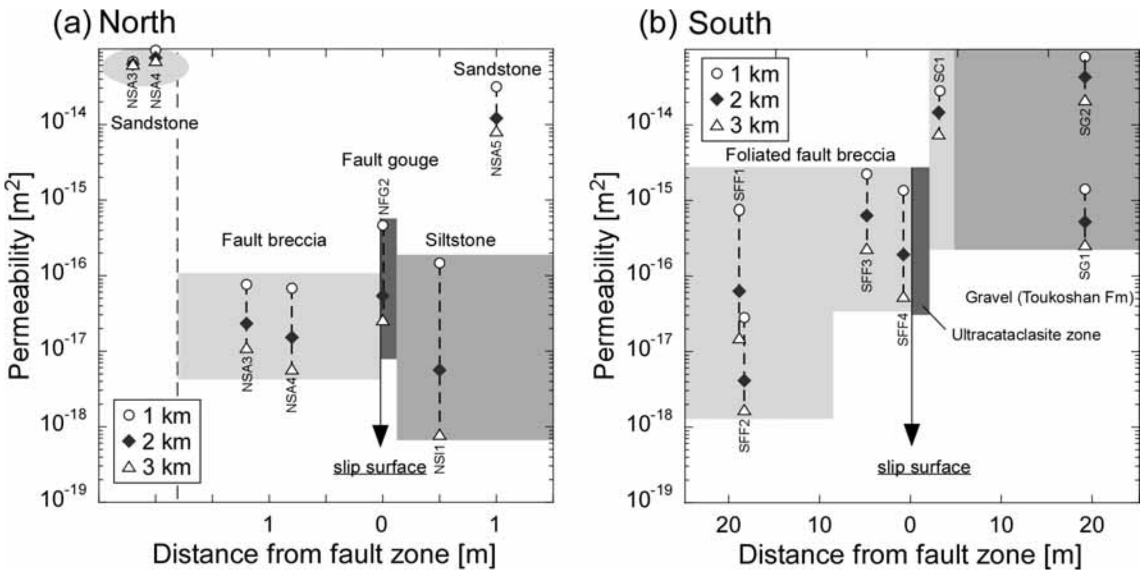

Figure 7. Permeability distributions at depths from 1 to 3 km around the slip zone at (a) the northern shallow borehole site and (b) the southern shallow borehole site.

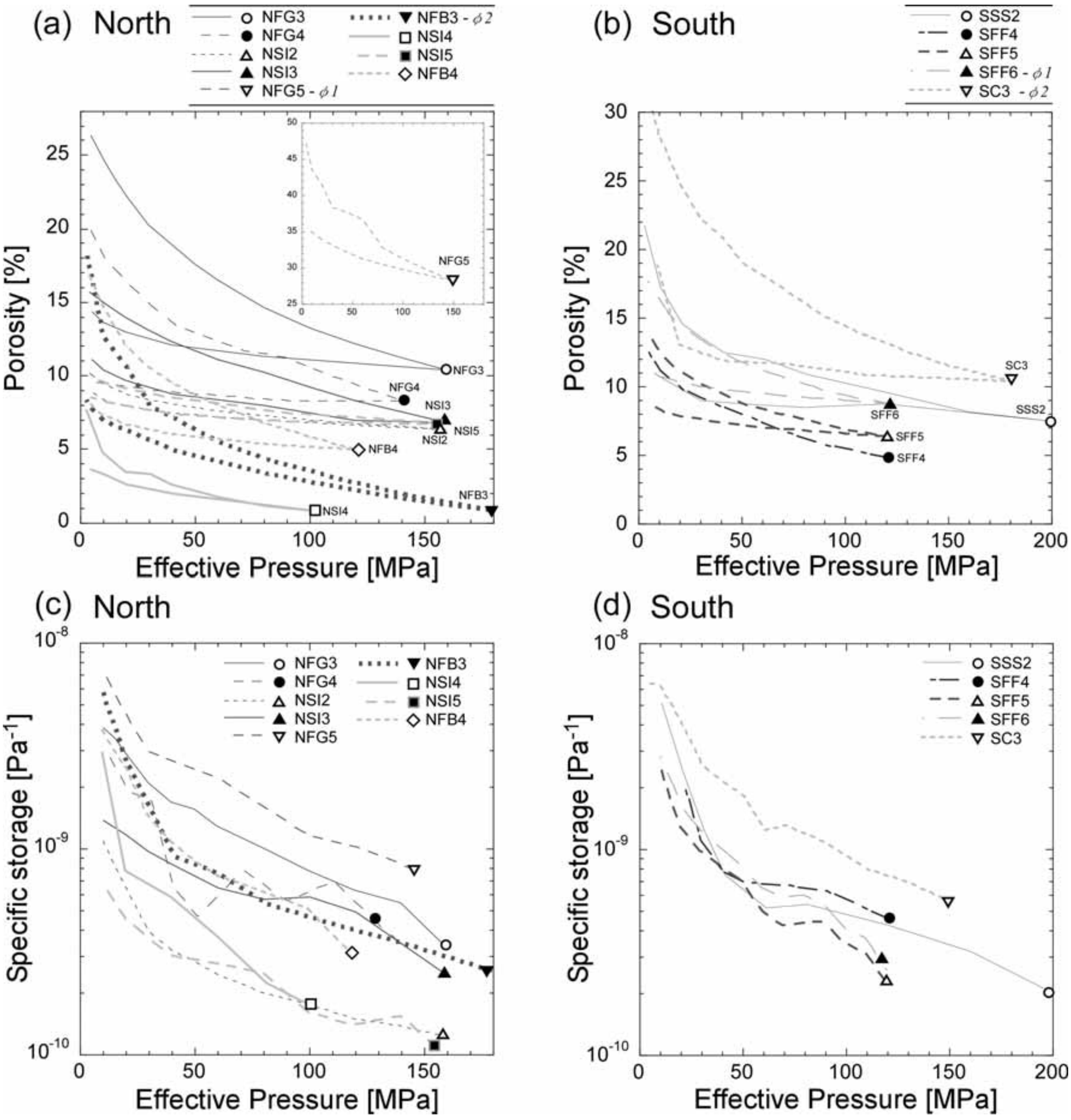

Figure 8. Porosity as a function of effective pressure for (a) the northern and (b) the southern shallow borehole samples. Specific storage as a function of effective pressure for (c) the northern and (d) the southern shallow borehole samples. Specific storage was determined from porosity data shown in Figure 8a and 8b. Drained pore compressibility was estimated from porosity. *Φ1* and *Φ2* are the porosities of the slip zone and the surrounding rock, respectively, which were used for thermal pressurization analysis.

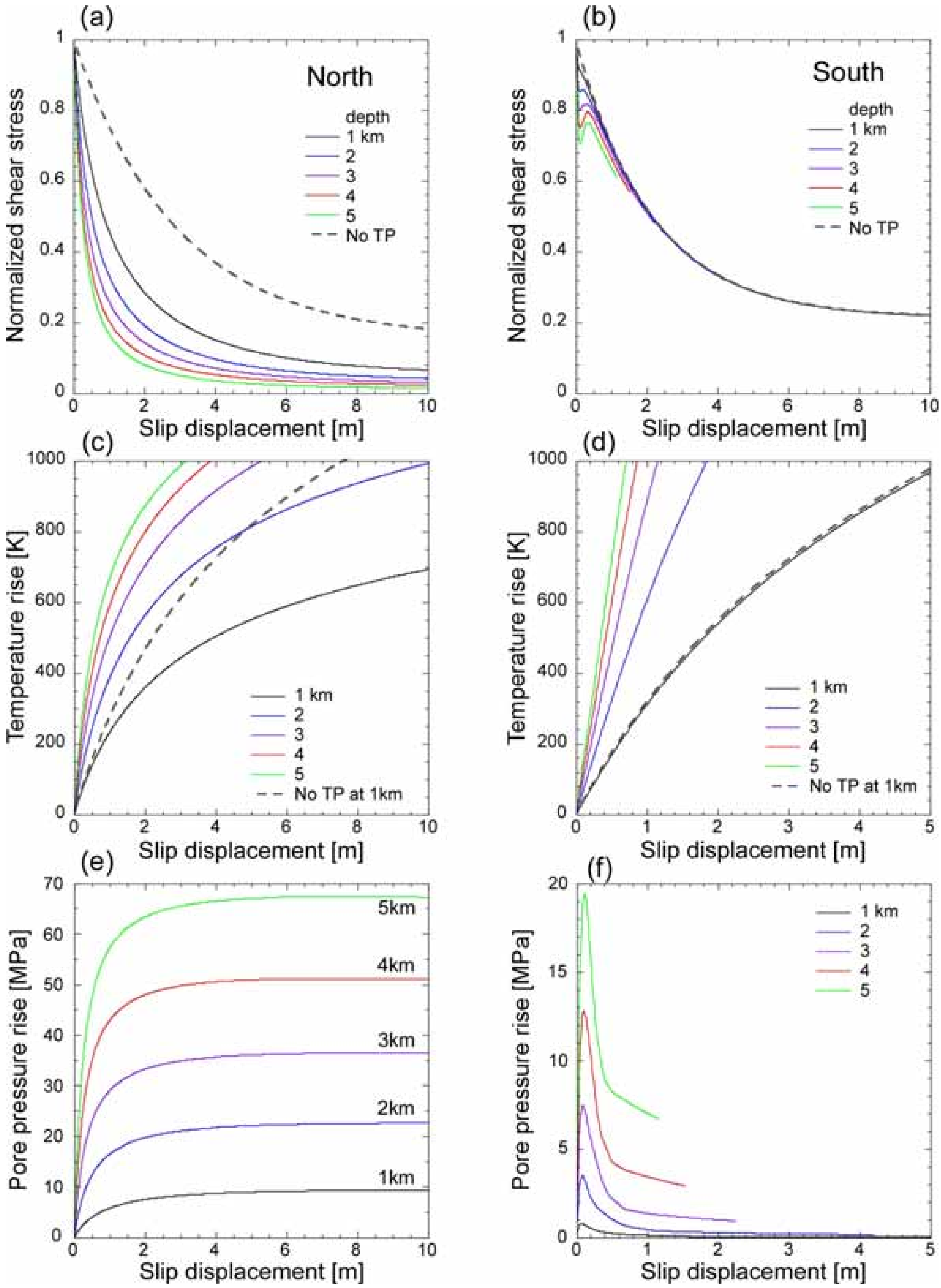

Figure 9. Shear stress evolution curves vs. slip displacement associated with thermal pressurization calculated at various depths for (a) the northern and (b) the southern

shallow borehole site. A one-dimensional finite-difference calculation based on the theory of *Lachenbruch* (1980) was performed using measured permeability and storage capacity values as a function of effective pressure along with friction data from the high-velocity friction tests. Fault strength is shown as a normalized shear stress with respect to the initial shear stress, assuming that the shear stress depends on the effective normal stress and displacement as determined by the high-velocity friction tests. Estimated temperature rise at the center of the slip zone during slip at (c) the northern and (d) the southern shallow borehole site taking into account thermal pressurization process. Estimated pore pressure rise at the center of the slip zone at (e) the northern and (f) the southern shallow borehole site.

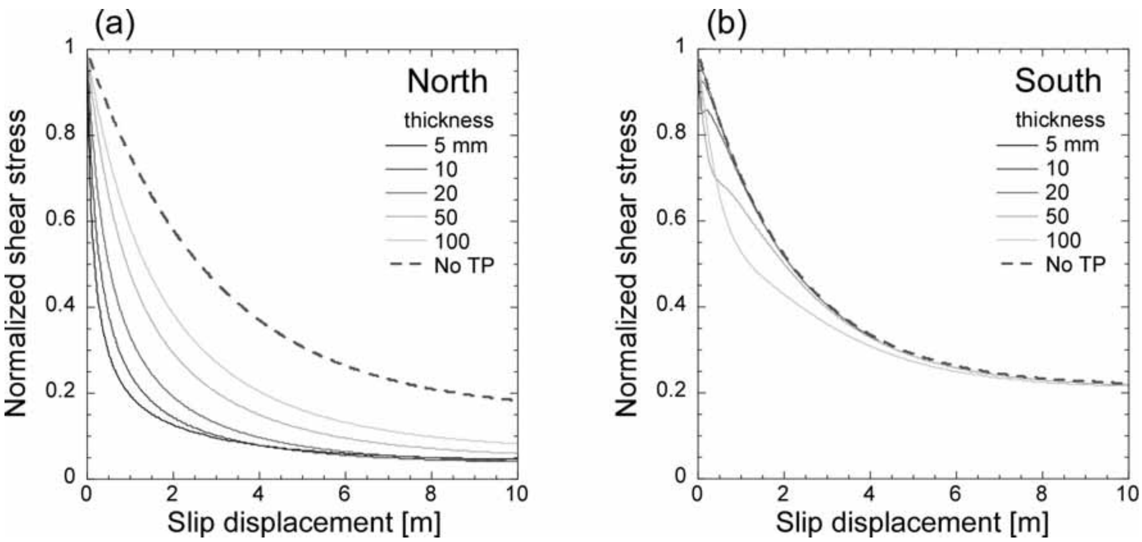

Figure 10. Shear stress evolution curves vs. slip displacement associated with thermal

pressurization calculated at 2 km depth and at various thickness of deformation zone for (a) the northern and (b) the southern shallow borehole site.

Symbol	Value	Units	Comment and Reference
α_f	5×10^{-4}	$℃^{-1}$	Coefficient of thermal expansibility of fluid (Luo & Vasseur 1992)
β_f	4.4×10^{-10}	Pa^{-1}	Compressibility of fluid (Luo & Vasseur 1992)
ρ_s	2500	$kg\ m^{-3}$	Bulk density of sediments
ρ_w	1000	$kg\ m^{-3}$	Density of water
T_0	20	℃	Surface temperature (z=0)
$\delta T/\delta z$	25	$K\ km^{-1}$	Geothermal gradient (Suppe & Wittke, 1977)
κ	2	$W\ m^{-1}\ K^{-1}$	Heat conductivity (Tanaka et al., 2006b)
c	800	$J\ kg^{-1}\ K^{-1}$	Heat capacity (Tanaka et al., 2006b)

Table 1. Physical parameters used for thermal pressurization analysis.

Sample	Well	Depth [m]	Rock type	Formation	Method	Pc [MPa]	Pp [MPa]	Permeability [m^2] / Porosity [%] during pressurizing path							Parameter used for TP analysis
								Pe	10 [MPa]	20	30	40	50	60	
Permeability															
NSA1	N	40.5	Sandstone	Chinshui	OPP	50-202	20		—	—	1.7E-15	6.8E-16	9.4E-17	1.7E-17	
NSA2	N	40.5	Sandstone	Chinshui	SSF	5.5-101	0.1-1		5.2E-15	3.2E-15	1.9E-15	5.7E-16	2.0E-16	4.6E-17	
NGF1	N	51	Fault gouge	Chinshui	SSF	2.9-140.6	0.1-1.1		2.3E-15	6.0E-16	3.2E-16	2.0E-16	9.5E-17	—	
NSA3	N	283	Sandstone	Kueichulin	SSF	2.1-202	0.05-0.8		4.7E-14	4.5E-14	4.4E-14	4.1E-14	4.3E-14	4.2E-14	
NSA4	N	283	Sandstone	Kueichulin	SSF	3.9-201.2	0.1-0.8		5.6E-14	5.0E-14	4.8E-14	4.7E-14	4.5E-14	—	
NFG1	N	305.5	Fault gouge	Kueichulin	SSF/OPP	3.3-80.4/101.5-170.4	0.1-0.7/20		3.7E-16	1.3E-16	3.9E-17	1.6E-17	—	4.5E-18	*k1*
NFB1	N	326.5	Fault breccia	Kueichulin	SSF	5-160	0.4-1.6		1.1E-16	4.5E-17	2.4E-17	1.1E-17	—	5.3E-18	*k2*
NFB2	N	326.5	Fault breccia	Kueichulin	SSF/OPP	3.1-30.8/51.4-199.6	0.1-0.6/20		4.0E-17	2.2E-17	8.0E-18	5.1E-18	—	2.3E-18	
NSA5	N	355.5	Sandstone	Kueichulin	SSF	3.2-199.1	0.1-1		1.0E-14	7.5E-15	6.3E-15	5.6E-15	5.0E-15	4.6E-15	
NSI1	N	402.5	Siltstone	Kueichulin	SSF/OPP	3-30.8/60.2-121.9	0.1-0.7/20		2.4E-16	3.6E-17	1.1E-17	1.7E-18	—	1.1E-19	
NFG0	—	0	Fault gouge	Chinshui	SSF/OPP	3.4-80.3/100.5-198	0.2-2/20		1.2E-15	3.4E-16	7.2E-17	2.1E-17	9.5E-18	3.9E-18	
SSS1	S	30	Sheared sandstone	Chinshui	SSF	2.9-199.5	0.2-0.7		1.7E-15	9.9E-16	6.9E-16	5.5E-16	3.9E-16	—	
SFF1	S	156.5	Foliated fault breccia	Chinshui	SSF	5-120	0.2-1.8		1.6E-15	2.6E-16	6.4E-17	2.1E-17	1.0E-17	4.3E-18	
SFF2	S	156.5	Foliated fault breccia	Chinshui	SSF/OPP	2.8-21.2/30-142.5	0.2-0.7/20		4.5E-17	1.5E-17	4.1E-18	2.0E-18	1.3E-18	—	
SFF3	S	173.5	Foliated fault breccia	Chinshui	SSF	3.1-110.8	0.2-0.8		2.7E-15	6.6E-16	1.9E-16	7.7E-17	3.6E-17	1.7E-17	*k1*
SC1	S	178	Clay	Toukoshan	SSF	2.9-181	0.1-0.5		3.4E-14	2.3E-14	1.5E-14	9.0E-15	6.1E-15	4.6E-15	*k2*
SC2	S	180	Clay	Toukoshan	SSF	3.5-25	0.1-1		1.9E-17	3.4E-18	7.1E-19	—	—	—	
SG1	S	194	Gravel (clay matrix)	Toukoshan	SSF	3-199.7	0.2-1.8		2.7E-15	8.5E-16	5.3E-16	3.0E-16	2.2E-16	1.6E-16	
SG2	S	194	Gravel (clay matrix)	Toukoshan	SSF	2.5-81.6/100.5-198	0.2-1/20		9.2E-14	6.6E-14	4.4E-14	2.6E-14	1.8E-14	1.3E-14	

Porosity													
NFG3	N	51	Fault gouge	Chinshui	5-160.5	0.6-0.7	24.8	22.2	20.3	19.0	17.7	16.5	
NFG4	N	51	Fault gouge	Chinshui	2.9-140.6	0.3	17.9	16.3	14.8	13.5	13.8	—	
NSI2	N	144	Siltstone (with sand layer)	Chinshui	5-160.5	0.65	9.5	8.8	8.4	8.1	7.9	7.6	
NSI3	N	299	Siltstone	Kueichulin	5-160.6	0.55-0.6	15.0	13.9	13.1	12.4	—	11.1	
NFG5	N	305	Fault gouge	Kueichulin	3.3-80.4/101.5-170.4	0.3/21	43.5	41.5	38.3	37.9	—	36.7	*ϕ1*
NFB3	N	326.5	Fault breccia	Kueichulin	3.1-30.8/51.4-199.6	0.3/20	12.7	10.5	7.9	7.1	—	5.5	*ϕ2*
NSI4	N	402.5	Siltstone	Kueichulin	3-30.8/60.2-121.9	0.3/20	4.8	3.4	3.3	2.6	—	1.7	
NSI5	N	402.5	Siltstone	Kueichulin	5-160.5	0.62	9.6	9.1	—	—	8.5	8.1	
NFB4	N	415	Fault breccia	Kueichulin	5-120.6	0.6-0.7	14.8	12.1	10.6	9.5	8.7	8.0	
SSS2	S	30	Sheared sandstone	Chinshui	2.9-199.5	0.3	17.2	14.5	13.5	12.5	—	12.0	
SFF4	S	156.5	Foliated fault breccia	Chinshui	2.8-21.2/30-142.5	0.3/20	11.1	9.8	9.2	8.5	7.9	—	
SFF5	S	167.2	Foliated fault breccia	Chinshui	5.6-120.8	0.9-1	12.8	11.2	10.2	9.5	8.8	8.3	
SFF6	S	170	Foliated fault breccia	Chinshui	5.6-120.6	0.95-1.1	16.4	14.6	13.4	12.6	11.8	11.2	*ϕ1*
SC3	S	178	Clay	Toukoshan	2.9-181	0.3	28.2	24.7	22.1	20.8	18.9	18.0	*ϕ2*

Table 2. Summary of the results of permeability and porosity measurements on core samples from the northern and the southern shallow holes. OPP: oscillating pore pressure method; SSF: steady state gas flow method. NFG0 is an outcropped sample at Ta-Chia River near Shihkang Dam.

	μ_r	μ_i	d_C	χ_0 [10^{-8} m^3/kg]	χ_{hvr}
North	0.15	0.95	8.8	10.8	3.5
South	0.22	1.03	6.4	23.7	30.1

Table 3. Fitting parameters of dynamic friction in equation (7) used for thermal pressurization analysis, and bulk magnetic susceptibilities before (χ_0) and after (χ_{hvr}) high-velocity friction test. Bulk magnetic susceptibility was measured with a KLY-3S Spinner Kappabridge (AGICO, Czech Republic ltd.).